CrossMark

Mesh sensitivity in peridynamic simulations

Steven F. Henke *, Sachin Shanbhag

Department of Scientific Computing, Florida State University, Tallahassee, FL 32306, USA

ARTICLE INFO

ABSTRACT

In this work, we investigate the suitability of several meshing strategies for use with a common peridynamics solution scheme. First, we use a manufactured solution to quantify the influence of different meshes on the accuracy and conditioning of a nonlocal boundary value problem in one and two dimensions. We explore convergence behavior, the effects of model parameters, and sensitivity to perturbations. We then apply the same meshing strategies to a three-dimensional impact simulation that employs the full peridynamic mechanical theory. We present a qualitative comparison of the fracture patterns that result, and suggest best practices for generating meshes that lead to efficient, high-quality numerical simulations of peridynamic models.

1. Introduction

Peridynamics [1–3] is a generalization of the classical theory of continuum mechanics to include nonlocal force interactions. The spatial extent of these interactions provides an intrinsic length, resulting in models that exhibit a scale-dependent response to applied stimuli. Balance laws and constitutive relations are formulated using integrals (rather than spatial derivatives which are only defined on smooth fields), so the formation and evolution of discontinuities, such as cracks, boundaries, and interfaces, can be controlled by a single constitutive relation. These features enable models that reproduce many complex materials phenomena, including fracture, failure modes in composites, and phase transitions. In the same spirit of the mechanical theory, an entire nonlocal calculus is under development [4,5] for general scalar, vector, and tensor quantities.

Due to the finite nature of computing machines, peridynamic simulations are prone to subtle computational difficulties. An appreciable source of such difficulties is the computational mesh, which represents the model geometry, and in many solution schemes, is invoked as part of a quadrature rule that resolves interactions near each material point. At present, guidance on generating meshes that are appropriate for peridynamic problems is tenuous, and best practices are not established for irregular meshes, which are desirable for their versatility and efficiency in

representing complex geometries. These details present sources for computation error and motivate the present study, where we systematically explore the relationship between model parameters and the underlying spatial discretization in an attempt to improve the fidelity of nonlocal simulations.

Several techniques, such as direct quadrature methods [6–9] and finite element methods [7,10,11], have been proposed for approximating solutions to this class of nonlocal models. The efficiency and accuracy of these approaches relies intimately on a discrete representation of the model geometry that tracks or captures the deformation of continuum bodies, including the location of any discontinuous features that may develop during the simulation. When present, discontinuities are constrained to follow contours of the mesh. As a result, the local resolution limits our knowledge of the position of discontinuities, and presents a restriction on the family of configurations that can be realized for that system. As a complement to mesh refinement procedures, which have been discussed by others [12,13], this work examines how irregular point placement strategies affect the accuracy of these computations and alleviates some obvious mesh dependent behaviors that have been observed. Previous studies have focused on other numerical issues in the peridynamic setting, including the performance of finite element meshes in the presence of stationary jump discontinuities [11], crack propagation and branching behavior [14], and symmetry breaking in dynamic fracture [15].

We first study mesh sensitivity in the simplified setting of a nonlocal boundary value problem (Section 2), where a manufactured solution enables a quantitative evaluation of discretization errors and conditioning. There, we identify primary error sources and examine the robustness of quadrature schemes to small

* Corresponding author. Tel.: +1 7155849882.
E-mail addresses: sfh07e@my.fsu.edu, shenke@fsu.edu (S.F. Henke), sshanbhag@fsu.edu (S. Shanbhag).

disturbances in the placement of grid points. In addition to the widely-used tensor product grids, we demonstrate that the generators of a centroidal Voronoi tessellation (CVT) bear desirable properties for integrating peridynamic interactions. Lessons from the scalar problem are then applied (Section 3) towards understanding meshing issues in a three-dimensional impact simulation that utilizes the full peridynamic mechanical theory. Qualitative aspects of the resulting fracture patterns are discussed and explanation of the observed behavior is attempted. We conclude (Section 4) with a summary of our findings and some suggestions for future investigations.

2. Nonlocal boundary value problem

As an initial attempt at understanding mesh sensitivity in peridynamic systems, we study meshing issues in a simpler, related context: the nonlocal "elliptic" boundary value problem. Using a manufactured solution and direct quadrature method, we explore the response of the discrete system to different quadrature point positioning strategies in one and two dimensions.

2.1. Nonlocal elliptic boundary value problem

A nonlocal elliptic boundary value problem [4,5,16] is governed by the balance equation,

$$b(\boldsymbol{x}) = \int_{\Omega} \gamma(\boldsymbol{x}, \boldsymbol{x}') \left(u(\boldsymbol{x}) - u(\boldsymbol{x}') \right) dV_{\boldsymbol{x}'}, \quad \forall (\boldsymbol{x}, \boldsymbol{x}') \in \Omega, \tag{1}$$

where $b(\boldsymbol{x})$ contains the known problem data, $\gamma(\boldsymbol{x}, \boldsymbol{x}')$ is a two-point modulus function that is symmetric in its arguments (i.e., $\gamma(\boldsymbol{x}, \boldsymbol{x}') = \gamma(\boldsymbol{x}', \boldsymbol{x})$), $u(\boldsymbol{x})$ is the unknown scalar quantity, and $V_{\boldsymbol{x}'}$ is the volume ascribed to the material point $\boldsymbol{x}'$. This equation is termed "elliptic", because it corresponds [16] with the spatial differential operator of the classical wave and diffusion equations, and nonlocal because the behavior at any point $\boldsymbol{x}$ within the domain depends on the behavior of points $\boldsymbol{x}'$ at a finite distance. Unlike its local counterpart, a constraint domain for nonlocal problems must have a measurable volume for well-posedness. Nonlocal versions of classical boundary conditions are obtained by specifying a function value (Dirichlet) or integral flux (Neumann) over a subset of the computational domain.

The strength of the interaction modulus typically decays with distance, so it is customary to truncate nonlocal interactions outside a finite region $\mathcal{H}_{\boldsymbol{x}} \subset \Omega$ surrounding each material point $\boldsymbol{x}$. That is,

$$\gamma(\boldsymbol{x}, \boldsymbol{x}') = 0 \quad \forall \boldsymbol{x}' \notin \mathcal{H}_{\boldsymbol{x}}. \tag{2}$$

This choice reduces the number of interactions that must be processed in simulating models, and supports a banded matrix structure in the discrete case. In this work, we assume that such a neighborhood exists, and is a ball,

$$\mathcal{H}_{\boldsymbol{x}} = \left\{ \boldsymbol{x}' \in \Omega : \|\boldsymbol{x} - \boldsymbol{x}'\| \le \delta \right\}, \tag{3}$$

parameterized by its radius δ, termed the peridynamic horizon. The local limit of δ provides correspondence with classical theories [5], and facilitates determining parameters in the modulus function. Changes to the horizon modify the relationship between these parameters (through a process called scaling [12,13]), and generally alters the dispersive properties of a medium [17]. Consequently, the cut-off radius is viewed as a constitutive parameter rather than a computational convenience. For more on physical and computational aspects involving the horizon see Refs. [6,11,17–19].

On the interior of the nonlocal region, we make the constitutive assumption that the modulus function is given by,

$$\gamma(\boldsymbol{x}, \boldsymbol{x}') = \|\boldsymbol{x}' - \boldsymbol{x}\|^{-P} \quad \forall \boldsymbol{x}' \in \mathcal{H}_{\boldsymbol{x}}, \tag{4}$$

where the nonlocal exponent P controls the strength profile of nonlocal interactions and affects the amount of smoothing [4] the integral operator imparts on the problem data. The form of Eq. (4) subsumes modulus functions found in a variety of settings, including micromechanics [1,2] ($P = 1$), mass and heat transport [20,21] ($P = 2$), and the fractional Laplacian [16,22] ($P = d + 2s$, where d is the spatial dimension and the parameter $0 < s < 1$). In problems where the domain is stationary, changing the value of P is equivalent to convolution of the integral operator with a spherical influence function [2,23].

2.2. Problem setup

For the computational experiments, we select a smooth manufactured solution that also appears in Ref. [11], and generalize it for multiple dimensions,

$$\hat{u}(\boldsymbol{x}) = R^2 - \|\boldsymbol{x}\|^2, \quad \forall \boldsymbol{x} \in \Omega \cup \Gamma, \tag{5}$$

where Ω is the solution domain and Γ the constraint domain. Direct substitution can be used to determine the forcing term that corresponds to this manufactured solution,

$$\hat{b}(\boldsymbol{x}) = \begin{cases} 2\delta^{3-P} / (3 - P) & d = 1, P < 3 \\ 2\pi \delta^{4-P} / (4 - P) & d = 2, P < 4, \end{cases} \tag{6}$$

which depends on the number of spatial dimensions d, nonlocal horizon δ, and nonlocal exponent P.

To facilitate a comparison with the impact problem that appears later in this paper, the solution domain Ω is chosen to be the ball-shaped region,

$$\Omega := \{\boldsymbol{x} : \|\boldsymbol{x}\| \le r\}, \tag{7}$$

that is enclosed by a constraint domain Γ, shaped like a spherical shell,

$$\Gamma := \{\boldsymbol{x} : r < \|\boldsymbol{x}\| \le R\}. \tag{8}$$

These domains are parameterized by an inner radius r and outer radius R, such that $r + \delta \le R$. Throughout the volume of the constraint region, we augment the governing equation with nonlocal Dirichlet data by enforcing the values,

$$u(\boldsymbol{x}) = \hat{u}(\boldsymbol{x}), \quad \forall \boldsymbol{x} \in \Gamma. \tag{9}$$

This setup effectively removes all boundaries and their associated difficulties (see [10,13,15]) from this research.

2.3. Solution method

Approximation of the governing equation (1) by a composite quadrature rule yields the discretization,

$$b(\boldsymbol{x}_i) \approx \sum_{j \ne i} \gamma(\boldsymbol{x}_i, \boldsymbol{x}_j) \left(u(\boldsymbol{x}_i) - u(\boldsymbol{x}_j) \right) V_j, \tag{10}$$

where all points positioned inside the computational domain are assigned an equal fraction of the region's analytical volume. This can be written as a linear system of equations,

$$\left[A(\boldsymbol{x}_i, \boldsymbol{x}_j) \right] \left[u(\boldsymbol{x}_j) \right] = \left[b(\boldsymbol{x}_i) \right], \tag{11}$$

where the entries of the system matrix are given by,

$$\left[A(\boldsymbol{x}_i, \boldsymbol{x}_j) \right] = \begin{cases} \sum_{j \ne i} \gamma(\boldsymbol{x}_i, \boldsymbol{x}_j) V_j & i = j \\ -\gamma(\boldsymbol{x}_i, \boldsymbol{x}_j) V_j & i \ne j. \end{cases} \tag{12}$$

(a) Manufactured solution.
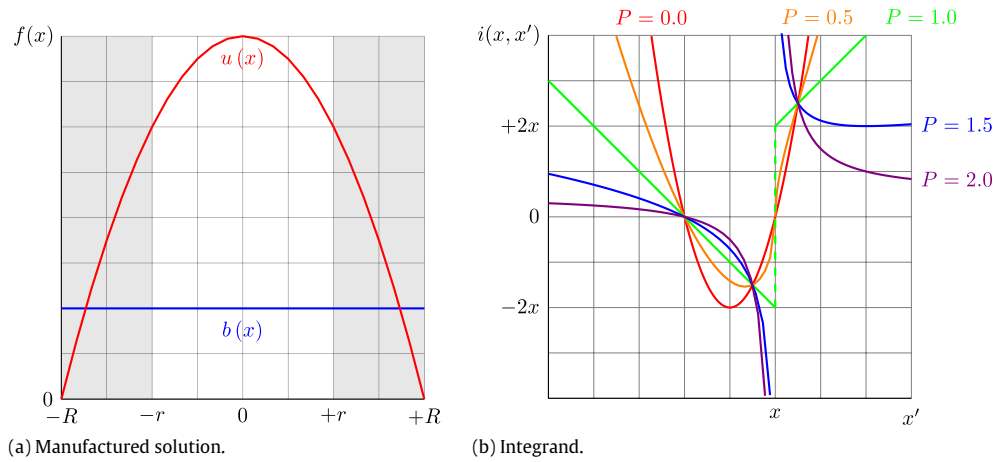
(b) Integrand.

Fig. 1. The uniform forcing term $b(\boldsymbol{x})$ yields the manufactured solution $\hat{u}(\boldsymbol{x})$. Substituting $\hat{u}(\boldsymbol{x})$ into the integrand $i(x, x')$ reveals the various limiting behaviors near $x' = x$ that are represented by this formulation.

This numerical method is occasionally termed "meshless" or "meshfree" because an explicit topological mesh is not required. For discussion, we still find it convenient to refer to the agglomeration of quadrature points that represent the computational domain as a mesh.

This discrete system is sparse whenever $\delta \ll r$, and is banded for certain node orderings. Accordingly, we obtain an approximate solution $\tilde{u}$ to Eq. (11) using the forcing term $\hat{b}$ and the LAPACK [24] banded solver dgbsvx,

$$\hat{b}(\boldsymbol{x}_i) = \sum_{j \neq i} \gamma(\boldsymbol{x}_i, \boldsymbol{x}_j)(\tilde{u}(\boldsymbol{x}_i) - \tilde{u}(\boldsymbol{x}_j)) V_j. \tag{13}$$

With the manufactured solution $\hat{u}$ in hand, we can also directly evaluate $\tilde{b}$, the result of the integral operator approximation,

$$\tilde{b}(\boldsymbol{x}_i) = \sum_{j \neq i} \gamma(\boldsymbol{x}_i, \boldsymbol{x}_j)(\hat{u}(\boldsymbol{x}_i) - \hat{u}(\boldsymbol{x}_j)) V_j. \tag{14}$$

Thus, the quality of the solutions we obtain is characterized using the absolute L_2 integration error (per node),

$$\epsilon_b = \frac{1}{N}\left(\sum_{i=1}^{N}\left|\tilde{b}(\boldsymbol{x}_i) - \hat{b}(\boldsymbol{x}_i)\right|^2 V_i\right)^{1/2}, \tag{15}$$

the absolute L_2 solution error (per node),

$$\epsilon_u = \frac{1}{N}\left(\sum_{i=1}^{N}\left|\tilde{u}(\boldsymbol{x}_i) - \hat{u}(\boldsymbol{x}_i)\right|^2 V_i\right)^{1/2}, \tag{16}$$

and the L_1 condition number estimate provided by the dgbsvx routine.

Throughout the numerical results presented here, the peridynamic horizon that we provide as input to our computer solution routines is revised to be slightly higher than the values we report here. We confirm that this adjustment, which is also mentioned in Ref. [25], was necessary for obtaining consistent results for our analysis. Without this change, particles at the edge of the nonlocal horizon were frequently excluded due to floating point errors. We found that a constant offset of 10^{-8} was sufficient for these purposes.

2.4. Numerical results for uniform meshes in 1-D

We begin studying the effects of meshing on the quality of peridynamic solutions in one dimension, where length is the only geometric construct that must be considered. This simplified setup provides insight into the behaviors observed in multiple dimensions, where geometry complicates the analysis. Here, we investigate how integration error, solution error, and conditioning are affected by the model parameters, uniform mesh refinement, and disturbances in the mesh regularity.

2.4.1. Manufactured solution

The manufactured solution and its corresponding forcing term possess the functional form of an inverted parabola and a positive constant value, respectively. These functions are plotted together in Fig. 1(a). Substituting the modulus function (4) and manufactured solution (5) into the governing equation (1), yields the piecewise integrand,

$$i(x, x') = \operatorname{sgn}(x' - x)(x' + x)|x' - x|^{1-P}, \tag{17}$$

shown for several values of P in Fig. 1(b). The nature of the singularity in this integrand changes depending on the value of P relative to $P = 1$,

$$\lim_{x' \to x} i(x, x') = \begin{cases} +\infty, & P > 1, \; x' > x \\ +2x, & P = 1, \; x' > x \\ 0, & P < 1 \\ -2x, & P = 1, \; x' < x \\ -\infty, & P > 1, \; x' < x, \end{cases} \tag{18}$$

where the term enclosed by the absolute value transitions between the numerator and the denominator. Thus, the singularity at $x' = x$ is removable when $P < 1$, has a jump that grows with x when $P = 1$, and is infinite whenever $P > 1$.

2.4.2. Convergence behavior

We demonstrate the convergence behavior of the direct integration method by overlaying the computational domain with a uniform grid of quadrature points. This quadrature scheme uses the same sample points to resolve both the nonlocal horizon and the geometry of the body, so the grid spacing is chosen proportionate to the peridynamic horizon (i.e. $\Delta x = \delta/m$, for some $m \geq 1$). The appropriate value for this mesh resolution parameter has been a subject of debate (see [6,9,11–15]). In these discussions, the values $m = 3$ and $m = 4$ are frequently suggested as a balance between accuracy and computational work for a particular horizon. In anisotropic materials, even larger m-values may be required [26,27]. To explore the effects of uniform mesh refinement on the system we have defined, we plot its integration error, solution error, and reciprocal condition number over a range of m in Fig. 2.
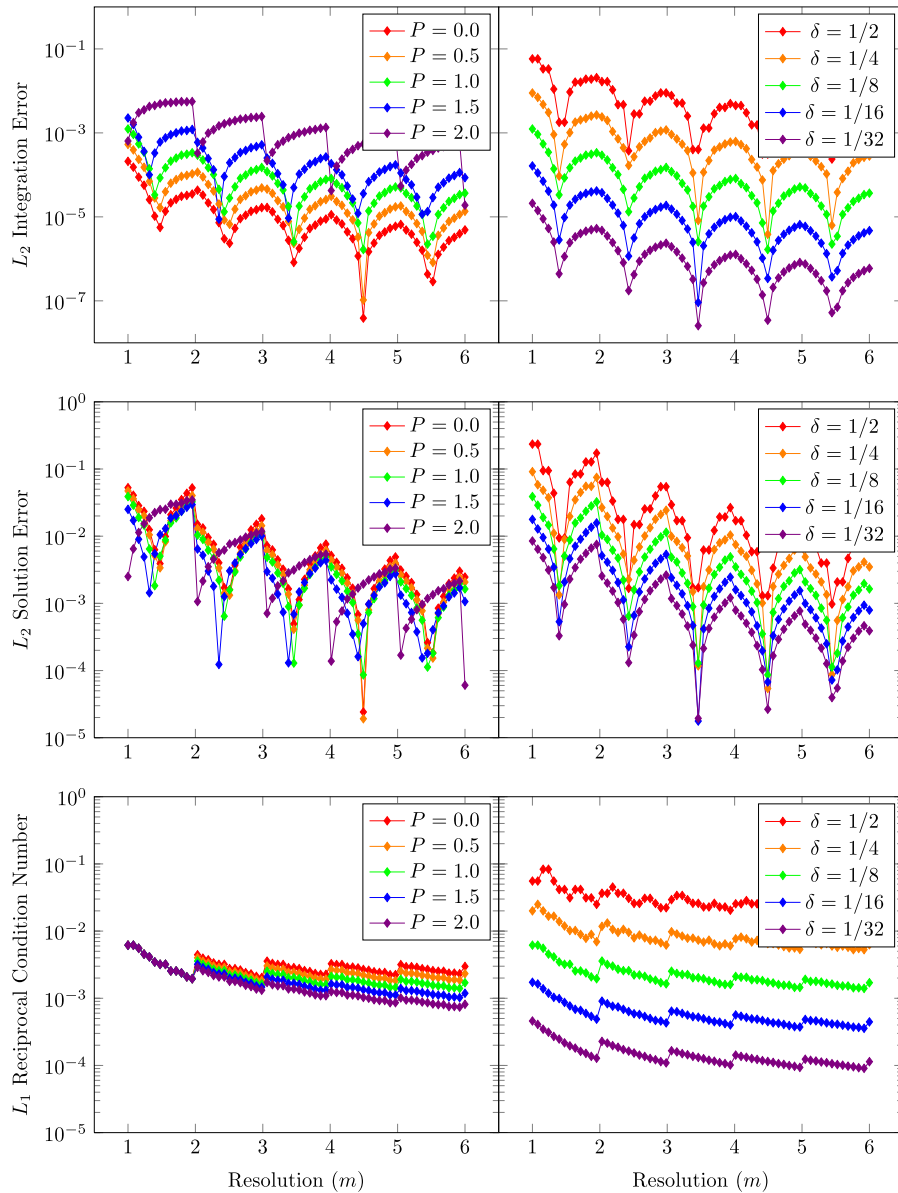
Fig. 2. Parameter study of the nonlocal boundary value problem in one dimension (with $r = 1$, $R = 2$). Plots on the left have $P = \{0.0, 0.5, 1.0, 1.5, 2.0\}$, and the horizon $\delta = 1/8$ fixed. Plots on the right have $\delta = \{1/2, 1/4, 1/8, 1/16, 1/32\}$, and the exponent $P = 1$ fixed. The mesh resolution parameter m increases from left to right.

As the mesh resolution changes, we observe periodic patterns in all of the observed quantities. The plots containing the integration and solution errors exhibit similar cusped features at each abscissa, and the reciprocal condition number repeats in a sawtooth pattern. All patterns repeat across each unit interval of m. For $P \le 1$, the maximum integration and solution errors are achieved near integer resolutions, and the minimum errors near half-integer resolutions. As the nonlocal exponent is increased beyond $P = 1$, the value of m that achieves the minimum error approaches its floor until $P = 2$, when a sharp jump appears near every integer m. Reducing the nonlocal horizon is associated with lower integration and solution errors, and a larger condition number. The dominant trend is that larger values of m reduce discretization errors, as is necessary for convergence of the method. It is interesting to note the similarities between these results and those obtained in Ref. [28].

The observed periodic behavior is an artifact of how the solution scheme and mesh we have chosen interact. In this study, the primary error source is the approximation of the integral operator

with a quadrature rule. The integral approximation can be written as (see derivation in Appendix A),

$$b(x_i) = \left(\frac{\delta}{m}\right)^{3-P} \sum_{k=1}^{\lfloor m \rfloor} \left[(2i + k)\,|k|^{1-P} \right.$$
$$\left. - (2i + k - \lfloor m \rfloor - 1)\,|k - \lfloor m \rfloor - 1|^{1-P}\right], \quad (19)$$

where a uniformly spaced mesh (i.e. $x_i = i\Delta x$) is assumed. In this expression, the flooring of m in the summation limit accounts for the periodic behavior in Fig. 2, and reflects the manner with which peridynamic interactions are processed: In this solution scheme, the spatial region occupied by the continuum body is decomposed into subregions. The behavior of each subregion is assumed to be well-represented by the response of a single chosen material point. Interactions are recorded between material points whenever they are located inside a shared peridynamic horizon. Consequently, whenever a material point is placed slightly inside (outside) the nonlocal horizon, interactions are (are not) recorded for the entire subregion. Thus, this binary approach to interaction processing

Table 1
Mean and standard deviation of L_2 solution error for an equidistant one-dimensional grid subject to small uniform perturbations. The maximum perturbation distance ε is chosen as a fraction of the unperturbed mesh spacing $\Delta x = \delta/m$. ($R = 2.0$, $r = 1.0$, 64 trials).

δ	$\varepsilon/\Delta x$	$P = 0.0$	$P = 1.0$	$P = 2.0$
(a) Mesh resolution $m = 2$				
2^{-2}	–	$(0.00 \pm 0.00) \cdot 10^{+01}$	$(2.67 \pm 0.00) \cdot 10^{-02}$	$(2.62 \pm 0.00) \cdot 10^{-03}$
	2^{-2}	$(3.43 \pm 1.51) \cdot 10^{-02}$	$(2.28 \pm 0.95) \cdot 10^{-02}$	$(3.91 \pm 0.78) \cdot 10^{-02}$
	2^{-3}	$(3.33 \pm 1.83) \cdot 10^{-02}$	$(2.22 \pm 1.12) \cdot 10^{-02}$	$(3.85 \pm 0.89) \cdot 10^{-02}$
	2^{-4}	$(2.89 \pm 1.78) \cdot 10^{-02}$	$(1.94 \pm 1.10) \cdot 10^{-02}$	$(3.66 \pm 0.83) \cdot 10^{-02}$
2^{-3}	–	$(1.73 \pm 0.00) \cdot 10^{-02}$	$(1.20 \pm 0.00) \cdot 10^{-02}$	$(5.77 \pm 0.00) \cdot 10^{-04}$
	2^{-2}	$(1.21 \pm 0.54) \cdot 10^{-02}$	$(7.97 \pm 3.33) \cdot 10^{-03}$	$(1.61 \pm 0.26) \cdot 10^{-02}$
	2^{-3}	$(1.21 \pm 0.54) \cdot 10^{-02}$	$(7.99 \pm 3.43) \cdot 10^{-03}$	$(1.60 \pm 0.27) \cdot 10^{-02}$
	2^{-4}	$(1.26 \pm 0.51) \cdot 10^{-02}$	$(8.27 \pm 3.10) \cdot 10^{-03}$	$(1.63 \pm 0.23) \cdot 10^{-02}$
2^{-4}	–	$(8.07 \pm 0.00) \cdot 10^{-03}$	$(5.70 \pm 0.00) \cdot 10^{-03}$	$(1.35 \pm 0.00) \cdot 10^{-04}$
	2^{-2}	$(5.17 \pm 1.95) \cdot 10^{-03}$	$(3.36 \pm 1.16) \cdot 10^{-03}$	$(7.34 \pm 0.82) \cdot 10^{-03}$
	2^{-3}	$(5.52 \pm 1.51) \cdot 10^{-03}$	$(3.58 \pm 0.93) \cdot 10^{-03}$	$(7.48 \pm 0.69) \cdot 10^{-03}$
	2^{-4}	$(5.06 \pm 1.66) \cdot 10^{-03}$	$(3.27 \pm 1.04) \cdot 10^{-03}$	$(7.26 \pm 0.81) \cdot 10^{-03}$
(b) Mesh resolution $m = 4$				
2^{-2}	–	$(1.14 \pm 0.00) \cdot 10^{-02}$	$(7.48 \pm 0.00) \cdot 10^{-03}$	$(6.03 \pm 0.00) \cdot 10^{-04}$
	2^{-2}	$(3.72 \pm 1.80) \cdot 10^{-03}$	$(2.43 \pm 1.21) \cdot 10^{-03}$	$(6.37 \pm 0.95) \cdot 10^{-03}$
	2^{-3}	$(3.83 \pm 1.65) \cdot 10^{-03}$	$(2.50 \pm 1.12) \cdot 10^{-03}$	$(6.41 \pm 0.91) \cdot 10^{-03}$
	2^{-4}	$(3.70 \pm 1.65) \cdot 10^{-03}$	$(2.39 \pm 1.10) \cdot 10^{-03}$	$(6.27 \pm 0.90) \cdot 10^{-03}$
2^{-3}	–	$(5.17 \pm 0.00) \cdot 10^{-03}$	$(3.48 \pm 0.00) \cdot 10^{-03}$	$(0.00 \pm 0.00) \cdot 10^{+01}$
	2^{-2}	$(1.27 \pm 0.57) \cdot 10^{-03}$	$(8.30 \pm 3.76) \cdot 10^{-04}$	$(2.81 \pm 0.27) \cdot 10^{-03}$
	2^{-3}	$(1.18 \pm 0.46) \cdot 10^{-03}$	$(7.67 \pm 3.07) \cdot 10^{-04}$	$(2.77 \pm 0.26) \cdot 10^{-03}$
	2^{-4}	$(1.27 \pm 0.52) \cdot 10^{-03}$	$(8.30 \pm 3.46) \cdot 10^{-04}$	$(2.78 \pm 0.29) \cdot 10^{-03}$
2^{-4}	–	$(2.46 \pm 0.00) \cdot 10^{-03}$	$(1.68 \pm 0.00) \cdot 10^{-03}$	$(3.30 \pm 0.00) \cdot 10^{-05}$
	2^{-2}	$(4.58 \pm 2.03) \cdot 10^{-04}$	$(2.93 \pm 1.33) \cdot 10^{-04}$	$(1.30 \pm 0.09) \cdot 10^{-03}$
	2^{-3}	$(4.63 \pm 1.97) \cdot 10^{-04}$	$(2.94 \pm 1.28) \cdot 10^{-04}$	$(1.30 \pm 0.09) \cdot 10^{-03}$
	2^{-4}	$(4.84 \pm 2.35) \cdot 10^{-04}$	$(3.07 \pm 1.53) \cdot 10^{-04}$	$(1.30 \pm 0.11) \cdot 10^{-03}$

introduces a systematic estimation error into the quadrature rule and results in the regular cusped features observed in Fig. 2. Had we properly accounted for the partial overlap of nonlocal volumes, the "serendipitous" error cancelation near half-integer values of m would likely not be observed, and the systematic over- or under-estimation of the integrand would be reduced. These inaccuracies directly influence the quality of the approximate solutions that are obtained.

2.4.3. Robustness to perturbations

One way to describe motion in time-dependent models is to allow the geometry representation to deform along with the continuum bodies it represents. This typically requires a temporal integration routine, and is accompanied by additional error sources. Such errors often result in minute changes in the relative distance between mesh points, thus affecting the accuracy of the spatial quadrature rule. In other cases, small perturbations may be introduced intentionally to break symmetries in the mesh (e.g. [9]). Using the same stationary solution as above, we examine statistically how these small errors in the location of quadrature points affect the accuracy of the numerical scheme.

For this investigation, we apply a uniform random perturbation to the position of all quadrature points in the initially equidistant discretization. The applied perturbation is small, and chosen relative to the initial lattice spacing, which provides an intrinsic length scale for the mesh. If the random disturbance places quadrature points outside the computational domain, the perturbation is rejected and generated again. The results of this study are displayed in Table 1, where we list the mean L_2 solution error and its standard deviation averaged over several independent trials. There, we also report the effects of controlled parameters through varying the maximum perturbation distance, mesh resolution parameter m, nonlocal horizon δ, and nonlocal exponent P.

Table 1 reveals the counterintuitive result that the presence of small random perturbations in the spacing of quadrature points,

on average, lowers solution errors for this one-dimensional problem. In all cases, error statistics show little sensitivity to the size of perturbations, demonstrating that small disturbances in quadrature point positions result in significant changes in accuracy. With all other factors held constant, increasing the mesh resolution m or decreasing the nonlocal horizon δ tends to reduce error. The effects of varying the nonlocal exponent P are not so straightforward. With a uniform discretization, solution errors decrease monotonically as P increases. However, when perturbations are introduced, simulations with $P = 1$ have the smallest error when all other parameters are held constant, followed by $P = 0$, then $P = 2$. In the next sections, we extend this analysis to two dimensions and demonstrate that many of these curious effects are unique to the one-dimensional problem.

2.5. Numerical results for square lattices in 2-D

The square tensor product grid is a straightforward generalization of the uniform one-dimensional mesh to multiple dimensions. With a second dimension, we now must consider both length and shape in our analyses. As a result, there are multiple ways to uniformly tile the disc that comprises our computational domain. We consider another approach to two-dimensional uniform grids in the next section.

2.5.1. Convergence behavior

Due to the additional structure of the added dimension, it is no longer possible to write a general mathematical expression that describes the error in our discrete integration and solution schemes. Following our work in one dimension, we begin with a study of mesh refinement, and plot the integration error, solution error, and condition number as the grid is refined.

In Fig. 3, we observe that the distinct periodic features that were characteristic of our one-dimensional study are no longer clearly visible. Changes to the value of the nonlocal exponent P no longer result in dramatic differences in the features of each series. Smaller
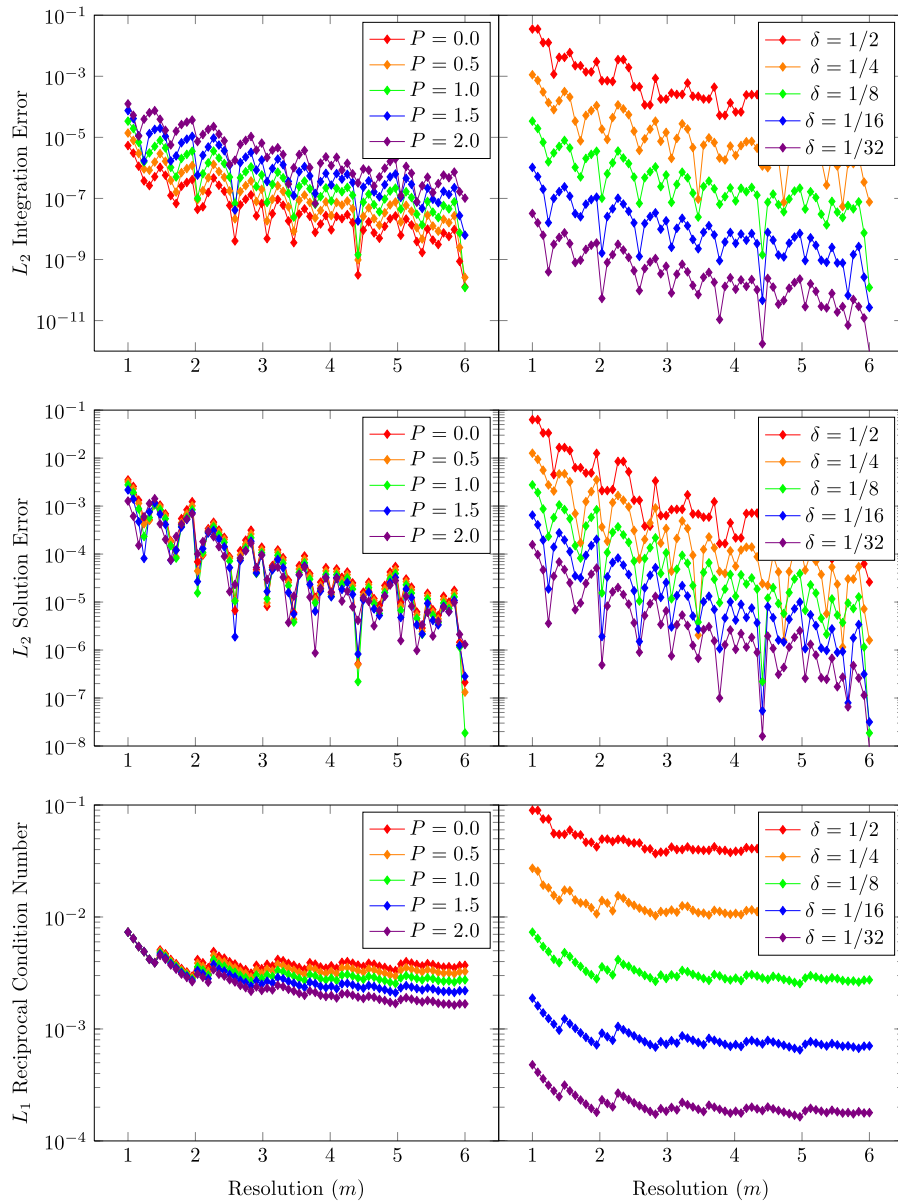
Fig. 3. Parameter study of the nonlocal boundary value problem in two dimensions (with $r = 1$, $R = 2$). Plots on the left have $P = \{0.0, 0.5, 1.0, 1.5, 2.0\}$, and the horizon $\delta = 1/8$ fixed. Plots on the right have $\delta = \{1/2, 1/4, 1/8, 1/16, 1/32\}$, and the exponent $P = 1$ fixed. The mesh resolution parameter m increases from left to right.

values of the nonlocal horizon δ continue to produce smaller errors, but larger condition numbers. Once again, the dominant trend is that increasing values of m reduce errors, demonstrating convergence for our method. We postulate that the noise that follows this downward trend is related to the systematic approximation errors described in the previous section, and the irregularity of these features can be attributed to the geometric incompatibility between the square grid and the rounded geometry of the nonlocal neighborhoods.

2.5.2. Robustness to perturbations

In two dimensions, random uniform perturbations applied to the placement of grid points (Table 2) tend to increase solution errors relative to their nominal values. Interestingly, the magnitude of these errors again appears to be insensitive to the size of the perturbation. This suggests that the higher order convergence that is associated with regular grids is fleeting, and may not be reliable for transient solution schemes that deform the grid. Convergence is again observed as the mesh resolution m increases or the

nonlocal extent δ decreases. A simple explanation for the behavior of the nonlocal exponent P is elusive. Ranked in order of increasing solution error, the most accurate models on perturbed grids for $m = 2$ are $P = 1$, $P = 2$, then $P = 0$. When $m = 4$ error decreases with increasing P. Computational issues involving modulus functions clearly warrant further study.

2.6. Numerical results for CVT generators in 2-D

The regularity of square tensor product grids may not always be desirable, especially in fracture simulations where cracks have a tendency to follow symmetry lines in the mesh. Motivated by a suggestion in Ref. [6], we study the effectiveness of meshes based on the generator points for a centroidal Voronoi tessellation (CVT) [29,30] which have previously been reported [31] to be high quality point sets for (local) meshless methods. CVT point distributions offer additional benefits, such as providing a more-faithful resolution of curved boundaries (thus avoiding the Cartesian staircase effect), attributing a meaningful volume to each

Table 2

Mean and standard deviation of L_2 solution error for a square two-dimensional grid subject to small uniform perturbations. The maximum perturbation distance ε is chosen as a fraction of the unperturbed mesh spacing $\Delta x = \delta/m$. ($R = 2.0$, $r = 1.0$, 64 trials).

δ	$\varepsilon/\Delta x$	$P = 0.0$	$P = 1.0$	$P = 2.0$
(a) Mesh resolution $m = 2$				
2^{-2}	–	$(6.89 \pm 0.00) \cdot 10^{-04}$	$(3.66 \pm 0.00) \cdot 10^{-04}$	$(2.28 \pm 0.00) \cdot 10^{-04}$
	2^{-2}	$(1.93 \pm 0.16) \cdot 10^{-03}$	$(1.51 \pm 0.11) \cdot 10^{-03}$	$(1.56 \pm 0.08) \cdot 10^{-03}$
	2^{-3}	$(1.95 \pm 0.16) \cdot 10^{-03}$	$(1.53 \pm 0.11) \cdot 10^{-03}$	$(1.57 \pm 0.07) \cdot 10^{-03}$
	2^{-4}	$(1.93 \pm 0.17) \cdot 10^{-03}$	$(1.51 \pm 0.12) \cdot 10^{-03}$	$(1.56 \pm 0.08) \cdot 10^{-03}$
2^{-3}	–	$(1.48 \pm 0.00) \cdot 10^{-04}$	$(7.48 \pm 0.00) \cdot 10^{-05}$	$(6.20 \pm 0.00) \cdot 10^{-05}$
	2^{-2}	$(4.51 \pm 0.15) \cdot 10^{-04}$	$(3.56 \pm 0.10) \cdot 10^{-04}$	$(3.70 \pm 0.07) \cdot 10^{-04}$
	2^{-3}	$(4.51 \pm 0.17) \cdot 10^{-04}$	$(3.56 \pm 0.11) \cdot 10^{-04}$	$(3.70 \pm 0.08) \cdot 10^{-04}$
	2^{-4}	$(4.46 \pm 0.18) \cdot 10^{-04}$	$(3.53 \pm 0.12) \cdot 10^{-04}$	$(3.68 \pm 0.08) \cdot 10^{-04}$
2^{-4}	–	$(0.00 \pm 0.00) \cdot 10^{+01}$	$(1.74 \pm 0.00) \cdot 10^{-05}$	$(1.53 \pm 0.00) \cdot 10^{-05}$
	2^{-2}	$(1.09 \pm 0.02) \cdot 10^{-04}$	$(8.61 \pm 0.12) \cdot 10^{-05}$	$(8.95 \pm 0.08) \cdot 10^{-05}$
	2^{-3}	$(1.09 \pm 0.02) \cdot 10^{-04}$	$(8.59 \pm 0.13) \cdot 10^{-05}$	$(8.94 \pm 0.09) \cdot 10^{-05}$
	2^{-4}	$(1.09 \pm 0.02) \cdot 10^{-04}$	$(8.61 \pm 0.15) \cdot 10^{-05}$	$(8.95 \pm 0.10) \cdot 10^{-05}$
(b) Mesh resolution $m = 4$				
2^{-2}	–	$(6.90 \pm 0.00) \cdot 10^{-05}$	$(5.55 \pm 0.00) \cdot 10^{-05}$	$(6.63 \pm 0.00) \cdot 10^{-05}$
	2^{-2}	$(2.19 \pm 0.03) \cdot 10^{-04}$	$(1.61 \pm 0.02) \cdot 10^{-04}$	$(1.34 \pm 0.01) \cdot 10^{-04}$
	2^{-3}	$(2.20 \pm 0.04) \cdot 10^{-04}$	$(1.61 \pm 0.03) \cdot 10^{-04}$	$(1.34 \pm 0.02) \cdot 10^{-04}$
	2^{-4}	$(2.19 \pm 0.04) \cdot 10^{-04}$	$(1.60 \pm 0.03) \cdot 10^{-04}$	$(1.34 \pm 0.02) \cdot 10^{-04}$
2^{-3}	–	$(1.61 \pm 0.00) \cdot 10^{-05}$	$(1.32 \pm 0.00) \cdot 10^{-05}$	$(1.58 \pm 0.00) \cdot 10^{-05}$
	2^{-2}	$(5.03 \pm 0.04) \cdot 10^{-05}$	$(3.73 \pm 0.03) \cdot 10^{-05}$	$(3.15 \pm 0.02) \cdot 10^{-05}$
	2^{-3}	$(5.04 \pm 0.05) \cdot 10^{-05}$	$(3.74 \pm 0.03) \cdot 10^{-05}$	$(3.16 \pm 0.02) \cdot 10^{-05}$
	2^{-4}	$(5.04 \pm 0.04) \cdot 10^{-05}$	$(3.74 \pm 0.03) \cdot 10^{-05}$	$(3.15 \pm 0.02) \cdot 10^{-05}$
2^{-4}	–	$(3.88 \pm 0.00) \cdot 10^{-06}$	$(3.18 \pm 0.00) \cdot 10^{-06}$	$(0.00 \pm 0.00) \cdot 10^{+01}$
	2^{-2}	$(1.21 \pm 0.00) \cdot 10^{-05}$	$(8.98 \pm 0.03) \cdot 10^{-06}$	$(7.63 \pm 0.02) \cdot 10^{-06}$
	2^{-3}	$(1.20 \pm 0.00) \cdot 10^{-05}$	$(8.98 \pm 0.03) \cdot 10^{-06}$	$(7.62 \pm 0.02) \cdot 10^{-06}$
	2^{-4}	$(1.20 \pm 0.00) \cdot 10^{-05}$	$(8.97 \pm 0.03) \cdot 10^{-06}$	$(7.62 \pm 0.02) \cdot 10^{-06}$

generator point, and offering the potential for adaptive refinement and non-uniform point densities.

Given a set of input points $\{z_i\}$ belonging to a domain Ω, a Voronoi region $\mathcal{V}_i$ contains all points in Ω that are closer to the generator point z_i than to any other generator z_j,

$$\mathcal{V}_i = \left\{ x \in \Omega : \|x - z_i\| < \|x - z_j\| \right.$$
$$\left. \forall j = 1, \ldots, N \text{ and } j \neq i \right\}. \tag{20}$$

The set $\{\mathcal{V}_i\}$ is a Voronoi diagram (or tessellation) of Ω. The mass centroid of a Voronoi region is defined by

$$z_i^* = \int_{\mathcal{V}_i} x \hat{\rho}(x) \, dV \bigg/ \int_{\mathcal{V}_i} \hat{\rho}(x) \, dV, \tag{21}$$

where the generator density function $\hat{\rho}(x)$, in general, differs from the physical mass density $\rho(x)$ that appears elsewhere in this work. When the generators coincide with the mass centers of the Voronoi regions,

$$z_i = z_i^* \quad \forall i = 1, \ldots, N, \tag{22}$$

the tessellation of Ω is a centroidal Voronoi tessellation. The construction of a CVT can be thought of as an optimization problem that seeks to reduce the distortion of the Voronoi regions, or equivalently, minimize the energy functional

$$\mathcal{E} = \sum_{i=1}^{N} \int_{\mathcal{V}_i} \hat{\rho}(x) \|x - z_i\|^2 \, dV. \tag{23}$$

This leads to a number of probabilistic and deterministic methods for computing CVTs that attempt to minimize Eq. (23) in some way.

In this work, we generate CVTs using a probabilistic variant of Lloyd's method. Lloyd's method [32] alternates between constructing Voronoi regions, and moving generator points the centroids

Table 3

L_2 solution error statistics for two-dimensional CVT meshes ($R = 2.0$, $r = 1.0$, 12 trials).

δ	$P = 0.0$	$P = 1.0$	$P = 2.0$
(a) Mesh resolution $m = 2$			
2^{-2}	$(2.49 \pm 0.34) \cdot 10^{-04}$	$(1.81 \pm 0.40) \cdot 10^{-04}$	$(5.90 \pm 0.51) \cdot 10^{-04}$
2^{-3}	$(5.07 \pm 1.61) \cdot 10^{-05}$	$(2.66 \pm 0.42) \cdot 10^{-05}$	$(1.20 \pm 0.13) \cdot 10^{-04}$
2^{-4}	$(1.12 \pm 0.21) \cdot 10^{-05}$	$(3.42 \pm 0.62) \cdot 10^{-06}$	$(2.76 \pm 0.13) \cdot 10^{-05}$
(b) Mesh resolution $m = 4$			
2^{-2}	$(4.54 \pm 0.81) \cdot 10^{-05}$	$(3.04 \pm 0.61) \cdot 10^{-05}$	$(1.29 \pm 0.39) \cdot 10^{-05}$
2^{-3}	$(1.08 \pm 0.10) \cdot 10^{-05}$	$(7.44 \pm 0.78) \cdot 10^{-06}$	$(2.03 \pm 0.48) \cdot 10^{-06}$
2^{-4}	$(2.73 \pm 0.33) \cdot 10^{-06}$	$(1.90 \pm 0.25) \cdot 10^{-06}$	$(3.53 \pm 1.57) \cdot 10^{-07}$

of their corresponding region. The variant we use is probabilistic because we sample the domain to determine region centroids without ever constructing the actual Voronoi diagram. We perform these iterations until the generators satisfy a convergence criterion. In this case, we require that no individual generator moves further than a distance of $\Delta x/32$, where Δx is the mesh spacing in the square Cartesian grid that we use to initialize the method. Once a mesh is within our chosen tolerance, we sample a final time to assign a volume to each generator. The volume we assign is the analytical volume of the domain scaled by the fraction of sample points that fall nearest each generator. A plot of the Voronoi regions for a square grid and a CVT grid on a disk-shaped domain are shown in Fig. 4.

2.6.1. Intrinsic variations

Centroidal Voronoi tessellations are not unique [29]. Table 3 summarizes the variation in solution error that is inherent in CVT point distributions manufactured to our chosen tolerance. It shows that, on average, solution errors and their standard deviations decrease as the extent of nonlocal interactions is reduced, or the mesh is refined. When $m = 2$, maximum accuracy is realized at

(a) Square grid.　　　　　　　　　　　　　　　　　(b) Centroidal Voronoi generators.
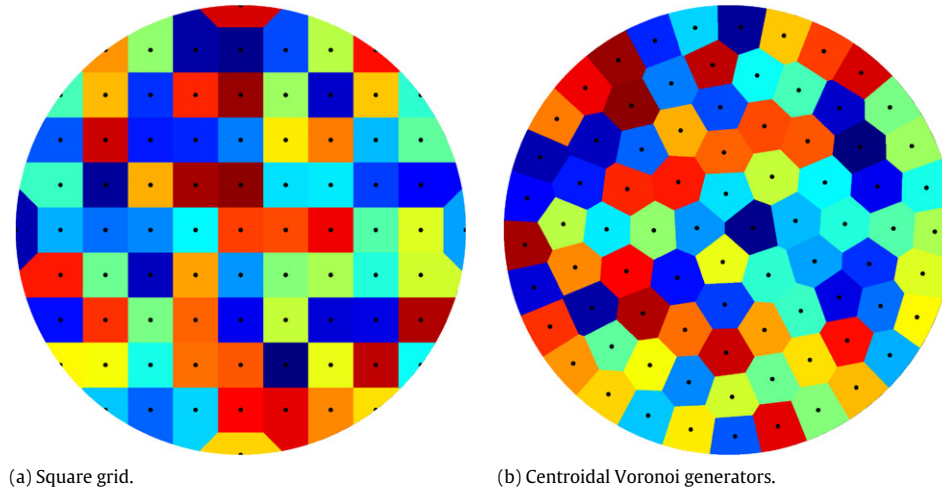
Fig. 4. Illustration of Voronoi regions of the two-dimensional grid types that are used in this work.

Table 4
Mean and standard deviation of L_2 solution error for a two-dimensional centroidal Voronoi generators subject to small uniform perturbations. The maximum perturbation distance ε is chosen as a fraction of the unperturbed mesh spacing $\Delta x = \delta/m$. ($R = 2.0$, $r = 1.0$, 64 trials.)

δ	$\varepsilon/\Delta x$	$P = 0.0$	$P = 1.0$	$P = 2.0$
(a) Mesh resolution $m = 2$				
2^{-2}	–	$(2.29 \pm 0.00) \cdot 10^{-04}$	$(1.83 \pm 0.00) \cdot 10^{-04}$	$(6.10 \pm 0.00) \cdot 10^{-04}$
	2^{-2}	$(2.32 \pm 0.15) \cdot 10^{-04}$	$(1.97 \pm 0.22) \cdot 10^{-04}$	$(6.22 \pm 0.26) \cdot 10^{-04}$
	2^{-3}	$(2.27 \pm 0.09) \cdot 10^{-04}$	$(1.85 \pm 0.15) \cdot 10^{-04}$	$(6.14 \pm 0.16) \cdot 10^{-04}$
	2^{-4}	$(2.25 \pm 0.04) \cdot 10^{-04}$	$(1.82 \pm 0.09) \cdot 10^{-04}$	$(6.11 \pm 0.10) \cdot 10^{-04}$
2^{-3}	–	$(0.00 \pm 0.00) \cdot 10^{+01}$	$(2.40 \pm 0.00) \cdot 10^{-05}$	$(1.12 \pm 0.00) \cdot 10^{-04}$
	2^{-2}	$(5.82 \pm 0.31) \cdot 10^{-05}$	$(2.33 \pm 0.09) \cdot 10^{-05}$	$(1.13 \pm 0.02) \cdot 10^{-04}$
	2^{-3}	$(5.78 \pm 0.23) \cdot 10^{-05}$	$(2.32 \pm 0.07) \cdot 10^{-05}$	$(1.13 \pm 0.02) \cdot 10^{-04}$
	2^{-4}	$(5.87 \pm 0.14) \cdot 10^{-05}$	$(2.35 \pm 0.05) \cdot 10^{-05}$	$(1.13 \pm 0.01) \cdot 10^{-04}$
2^{-4}	–	$(9.45 \pm 0.00) \cdot 10^{-06}$	$(3.66 \pm 0.00) \cdot 10^{-06}$	$(2.88 \pm 0.00) \cdot 10^{-05}$
	2^{-2}	$(9.51 \pm 0.28) \cdot 10^{-06}$	$(3.61 \pm 0.11) \cdot 10^{-06}$	$(2.88 \pm 0.02) \cdot 10^{-05}$
	2^{-3}	$(9.46 \pm 0.16) \cdot 10^{-06}$	$(3.63 \pm 0.07) \cdot 10^{-06}$	$(2.88 \pm 0.01) \cdot 10^{-05}$
	2^{-4}	$(9.52 \pm 0.12) \cdot 10^{-06}$	$(3.59 \pm 0.05) \cdot 10^{-06}$	$(2.88 \pm 0.01) \cdot 10^{-05}$
(b) Mesh resolution $m = 4$				
2^{-2}	–	$(5.44 \pm 0.00) \cdot 10^{-05}$	$(3.76 \pm 0.00) \cdot 10^{-05}$	$(8.03 \pm 0.00) \cdot 10^{-06}$
	2^{-2}	$(5.33 \pm 0.10) \cdot 10^{-05}$	$(3.67 \pm 0.08) \cdot 10^{-05}$	$(8.32 \pm 0.36) \cdot 10^{-06}$
	2^{-3}	$(5.35 \pm 0.06) \cdot 10^{-05}$	$(3.69 \pm 0.05) \cdot 10^{-05}$	$(8.26 \pm 0.21) \cdot 10^{-06}$
	2^{-4}	$(5.39 \pm 0.05) \cdot 10^{-05}$	$(3.71 \pm 0.04) \cdot 10^{-05}$	$(8.18 \pm 0.16) \cdot 10^{-06}$
2^{-3}	–	$(1.06 \pm 0.00) \cdot 10^{-05}$	$(7.25 \pm 0.00) \cdot 10^{-06}$	$(2.18 \pm 0.00) \cdot 10^{-06}$
	2^{-2}	$(1.06 \pm 0.01) \cdot 10^{-05}$	$(7.25 \pm 0.07) \cdot 10^{-06}$	$(2.18 \pm 0.05) \cdot 10^{-06}$
	2^{-3}	$(1.06 \pm 0.01) \cdot 10^{-05}$	$(7.28 \pm 0.05) \cdot 10^{-06}$	$(2.16 \pm 0.03) \cdot 10^{-06}$
	2^{-4}	$(1.06 \pm 0.01) \cdot 10^{-05}$	$(7.29 \pm 0.04) \cdot 10^{-06}$	$(2.16 \pm 0.02) \cdot 10^{-06}$
2^{-4}	–	$(3.08 \pm 0.00) \cdot 10^{-06}$	$(2.17 \pm 0.00) \cdot 10^{-06}$	$(2.06 \pm 0.00) \cdot 10^{-07}$
	2^{-2}	$(3.07 \pm 0.01) \cdot 10^{-06}$	$(2.17 \pm 0.01) \cdot 10^{-06}$	$(2.08 \pm 0.03) \cdot 10^{-07}$
	2^{-3}	$(3.07 \pm 0.01) \cdot 10^{-06}$	$(2.17 \pm 0.01) \cdot 10^{-06}$	$(2.08 \pm 0.02) \cdot 10^{-07}$
	2^{-4}	$(3.07 \pm 0.00) \cdot 10^{-06}$	$(2.17 \pm 0.00) \cdot 10^{-06}$	$(2.07 \pm 0.02) \cdot 10^{-07}$

$P = 1$, followed by $P = 0$ then $P = 2$. However, when $m = 4$ accuracy increases with P. Overall, the accuracy CVT distributions is similar to that of the perfect square lattice.

2.6.2. Robustness to perturbations

Following our investigation of regular Cartesian grids, Table 4 reports the statistics of small perturbations in a CVT point distribution. To clarify, we select a single representative mesh from the collection that was characterized in Table 3, and over several independent trials, we accumulate statistics of the errors that arise in response to applying uniform random displacements to the initial positions of all quadrature points. The number of quadrature points and lattice spacing correspond exactly with the square lattices studied in the previous section. This procedure reveals that

CVT point distributions are robust to small disturbances in quadrature point positions. In many cases, perturbations lower error, similar to the one-dimensional result. Identical tests were carried out for the other CVT point distributions, and the observed behaviors are consistent.

3. Peridynamic projectile impact

The impact of a brittle target by a high speed projectile has become a benchmark problem for peridynamics. In this section, we use the impact problem as a prototype for investigating how meshing affects fracture simulations. Although the state-based [2] theory enables a wider range of elastic responses, the simpler bond-based formulation of peridynamics is sufficient for the
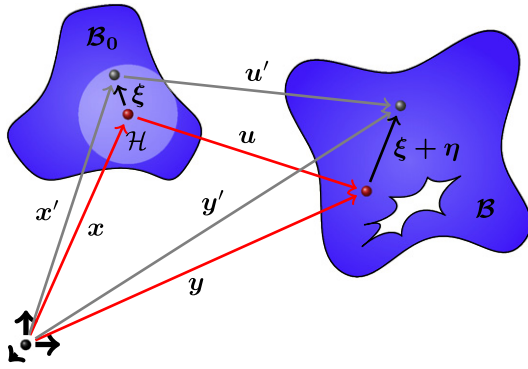
Fig. 5. Kinematic quantities that describe the motion of a peridynamic continuum body as it deforms from its reference configuration ($\mathcal{B}_0$) to its current configuration ($\mathcal{B}$).

purpose of the present investigation, and we use it here. The notation and model we summarize below is almost identical to the Refs. [6,9].

3.1. Peridynamic theory of solid mechanics

The peridynamic theory of mechanics is based on an integro-differential equation of motion,

$$\rho(\mathbf{x})\, \ddot{\mathbf{u}}(\mathbf{x}, t) = \int_{\mathcal{H}_{\mathbf{x}}} \mathbf{f}(\eta, \xi)\, dV_{\mathbf{x}'} + \mathbf{b}(\mathbf{x}, t), \tag{24}$$

where $\rho(\mathbf{x})$ is the mass density, $\mathbf{f}(\eta, \xi)$ is a pairwise force function, and $\mathbf{b}(\mathbf{x}, t)$ is a loading force density.

Relationships between the kinematic variables, including the mechanical displacement $\mathbf{u}(\mathbf{x}, t)$, relative reference position $\xi(\mathbf{x})$, and relative displacement $\eta(\mathbf{x}, t)$, are illustrated in Fig. 5. The definition of the nonlocal neighborhood that has already been given in Eq. (3) remains unchanged.

We employ the peridynamic microelastic brittle (PMB) [6] material model, in which bonded particles exert a force on each other that is analogous to that of an elastic spring,

$$\mathbf{f}(\eta, \xi) = cs\mu\, \frac{\eta + \xi}{\|\eta + \xi\|}. \tag{25}$$

Above, c is an elastic modulus, μ is a scalar damage function, and the bond stretch s is the change in length of a bond relative to its length in the reference configuration,

$$s = \frac{\|\xi + \eta\| - \|\xi\|}{\|\xi\|}. \tag{26}$$

The elastic modulus c is fixed by matching the peridynamic and classical energy expressions for a homogeneous deformation, where the theories coincide. This approach yields [6]

$$c = \frac{18K}{\pi \delta^4}, \tag{27}$$

where K is the bulk modulus of the elastic material.

In a brittle damage model, bonds stretched beyond a critical extension (denoted s_0) are broken irreversibly so that the particle pair no longer interacts,

$$\mu = \begin{cases} 1, & s(t') < s_0 \ \forall\, t' \in (0, t) \\ 0, & \text{otherwise}. \end{cases} \tag{28}$$

The chosen value for s_0 can be related to the fracture energy G_0 through the relation [6],

$$G_0 = \frac{\pi}{10} cs_0^2 \delta^5. \tag{29}$$
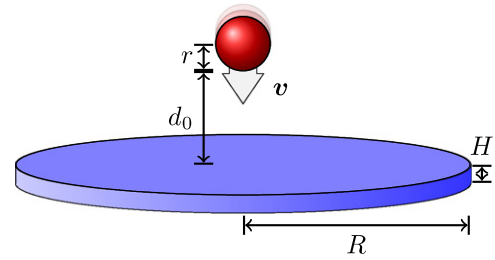
Fig. 6. The initial problem geometry consists of a high speed spherical projectile incident upon a cylindrical plate of the same composition.

A repulsive short-range force is introduced in the current configuration to prevent the overlap of moving material,

$$\mathbf{f}^{SR}(\eta, \xi) = g(\eta, \xi)\, \frac{\eta + \xi}{\|\eta + \xi\|}, \tag{30}$$

where the force magnitude is given by

$$g(\eta, \xi) = \min\left\{0, \frac{c^{SR}}{\delta}\left(\|\eta + \xi\| - d^{SR}\right)\right\} \tag{31}$$

as has been done in other work [9,10]. The short-range interaction modulus c^{SR} is nonzero over the distance,

$$d^{SR} = \min\left\{0.90\,\|\mathbf{x} - \mathbf{x}'\|,\, 1.35\left(\hat{r} + \hat{r}'\right)\right\}, \tag{32}$$

that depends on the relative position of material points in the reference configuration and the fixed node radii $\hat{r}$ and $\hat{r}'$.

3.2. Problem setup

The initial problem geometry (depicted in Fig. 6) consists of a high speed spherical projectile incident along the central longitudinal axis of a cylindrical plate. The impactor has radius $r = 0.45$ cm and speed $\|\mathbf{v}\| = 100$ m/s. The target has radius $R = 3.75$ cm and thickness $H = 0.30$ cm. The center of the projectile is displaced by a distance $d_0 = 0.18$ cm, which is slightly larger than $r + \delta$, from the top surface of the plate. Every node is assigned a radius $\hat{r} = 0.5$ cm, that is used in calculating non-bonded forces. As the simulation transpires, the impactor collides with the target with both sustaining damage. The simulation is terminated at the moment when the projectile, if unobstructed, would arrive at its mirror position on the opposite side of the plate.

The bodies are designated to have the same composition, with material parameters chosen identically to the Refs. [6,9,23]: the mass density $\rho = 2200$ kg m^{-3}, bulk modulus $K = 1.4900 \times 10^{10}$ N m^{-2}, and horizon $\delta = 5 \times 10^{-03}$ m. The chosen critical stretch value $s_0 = 5 \times 10^{-04}$ corresponds to a material with fracture energy $G_0 \approx 33.5$ J m^{-2}. As suggested in Ref. [10], the modulus for short range forces is selected so it is roughly equivalent to the bulk elastic modulus of the material, specifically $c^{SR} = 15c$.

Although our problem setup is shared with the Refs. [6,9,23], our implementation differs in several important ways. First, our projectile is modeled as a physical body that sustains damage during the course of the simulation. This approach requires short range forces to model contact and contrasts the idealized force field used in previous work. Second, we use a simplified bond-breaking criterion that is independent of the state of other bonds in the system, rather than the damage-dependent critical stretch suggested in [6,9]. Thus, material points that have sustained damage manifest a relatively weaker material (for more see [15]). Together, these factors account for the majority of discrepancies between the fracture patterns shown here, and those published in previous works.

Table 5
Effects of spatial and temporal refinement on damage patterns in the brittle impact problem. All simulations use a simple cubic grid and an impact velocity of 100 m/s.

	$\Delta t = 2.0 \times 10^{-8}$	$\Delta t = 1.0 \times 10^{-8}$	$\Delta t = 0.5 \times 10^{-8}$
$m = 2$	Avg. Damage 0.9739	Avg. Damage 0.4808	Avg. Damage 0.3646
$m = 3$	Avg. Damage 0.2985	Avg. Damage 0.2493	Avg. Damage 0.2386
$m = 4$	Avg. Damage 0.4054	Avg. Damage 0.4065	Avg. Damage 0.4090
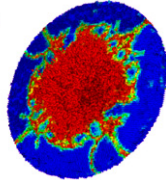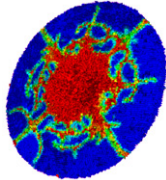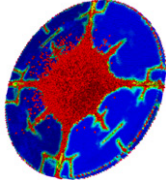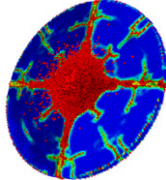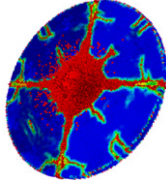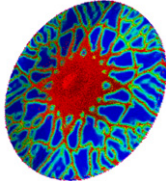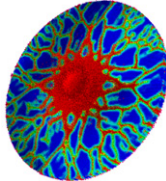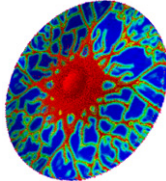
3.3. Solution method

We discretize the peridynamic equation of motion (24) using the mesh-free "EMU" method [6,9], which approximates spatial integrals using a composite quadrature rule,

$$\rho_i \ddot{\boldsymbol{u}}_i^n \approx \sum_{\boldsymbol{x}_j \in \mathcal{H}_{\boldsymbol{x}_i}} \boldsymbol{f}\left(\boldsymbol{u}_j^n - \boldsymbol{u}_i^n, \boldsymbol{x}_j - \boldsymbol{x}_i\right) V_j + \boldsymbol{b}_i^n, \tag{33}$$

and temporal derivatives using a central difference method,

$$\ddot{\boldsymbol{u}}_i^n = \frac{\boldsymbol{u}_i^{n+1} - 2\boldsymbol{u}_i^n + \boldsymbol{u}_i^{n-1}}{(\Delta t)^2} + \mathcal{O}\left((\Delta t)^2\right). \tag{34}$$

In these equations, superscripts denote the time step, and subscripts indicate the node where the quantity is evaluated. The error term in the spatial integration method is formally shown [6] to be $\mathcal{O}\left((\Delta x)^2\right)$ for smooth solutions, but reverts to $\mathcal{O}\left(\Delta x\right)$ in the presence of discontinuities. Throughout this section, our simulations internally use a slightly higher value of δ than we report (to alleviate numerical errors). The actual horizon used in these simulations is 1e−8 length units longer than the values stated here.

3.4. Numerical results

The results reported here detail an investigation into the factors that influence mesh dependent behavior. In the following, we present a parametric study of the impact problem and highlight qualitative differences in the fracture patterns that result from refining the domains, changing the impact velocity, and using irregular quadrature point distributions. Simulation runtimes are listed in Appendix B.

3.4.1. Spatial and temporal refinement effects

The impact model simulated in Ref. [9], was able to show that increasing the horizon at a fixed grid resolution leads to fracture patterns that deviate from the mesh symmetry axes. We assume the complementary view, that the horizon is a fixed constitutive parameter, and demonstrate how the uniform refinement of a cubic tensor product grid alters the outcome of the simulation (Table 5). Grid refinement techniques for peridynamic brittle fracture also appear in Refs. [14,15], where this mode of convergence is termed *m*-convergence [12,13]. Because spatial and temporal accuracy are linked within our solution scheme, the following results also display the effects of changing the time step length.

Corroborating the finding of Ref. [9], we observe that the level of spatial detail can strongly influence the obtained damage fields. The lowest resolution, $m = 2$, shows increasing damage as the iteration interval is lengthened. This likely occurs because the damage model, which has an implicit time-dependence in the bond stretch, is increasingly overwhelmed by the larger displacements that transpire. This strong response to time-step hints that the results with $m = 2$ may not be reliable. There is little evidence of time step sensitivity for $m = 3$, but the cracks that develop artificially concentrate along coordinate axes. Close inspection reveals that such fissures are caused by short range interactions between free particles. These particles at the center of the target debond at initial contact, and are directed outward along the coordinate axes. Because mesh points are aligned in rows, the free particles collide with and dislodge their neighbors in a repeating pattern that propagates to the edge of the target, bisecting it along the path. As a result, $m = 4$ is the coarsest spatial resolution that simultaneously yields fracture patterns that deviate from the mesh symmetry axes, and is insensitive to the time step duration. We also note that the

Table 6
Effects of impactor speed on damage patterns in the brittle impact problem. All simulations were carried out with the same number of quadrature points (corresponding to a simple cubic grid with $m = 3$) and time step $\Delta t = 10^{-8}$.

	Simple cubic	Perturbed simple cubic	Centroidal Voronoi generators
Speed 50 m/s	Avg. Damage 0.1727	Avg. Damage 0.1643	Avg. Damage 0.1905
Speed 100 m/s	Avg. Damage 0.2493	Avg. Damage 0.2032	Avg. Damage 0.3624
Speed 200 m/s	Avg. Damage 0.5643	Avg. Damage 0.5596	Avg. Damage 0.6050
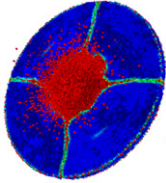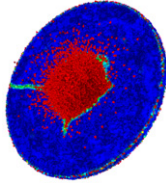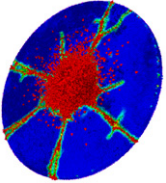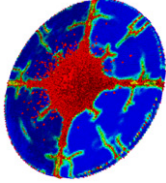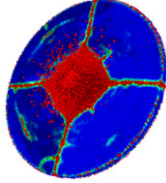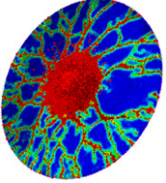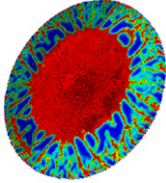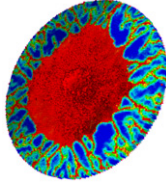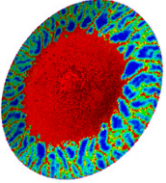
broken symmetry observed in all of the fracture patterns is a direct result of numerical errors in the solution scheme. A detailed explanation of this behavior was provided in Ref. [15].

3.4.2. Impact velocity effects

In addition to the iteration interval, temporal stability is also affected by the impact speed of the projectile. To understand this dependence, we repeat the simulations: first with the impact speed halved, then a second time with the impact speed doubled. While we have demonstrated favorable outcomes using a mesh resolution of $m = 4$, we concentrate here on the coarser mesh that has $m = 3$ and demands less computational work. Moreover, this choice provides an opportunity to investigate the axis-aligned cracking that was observed in the domain resolution study.

Existing solution schemes for peridynamic models have largely been based on cubic Cartesian meshes. As demonstrated, the regularity of these grids can introduce a directional bias into solutions, resulting in fracture patterns that artificially track symmetries in the mesh. To alleviate this behavior, it has been suggested [9] that small perturbations be applied to the mesh points "as a way of incorporating the inherent randomness in the distribution of defects in real materials". This idea can be generalized to fully irregular quadrature point distributions, such as the CVT generators that were introduced earlier in this work (see Section 2.6). CVT generators appear to be a promising alternative to tensor product grids because they achieve similar accuracy, yet possess a robustness to small position perturbations that the latter lacks. We continue by comparing the response of cubic Cartesian, perturbed cubic Cartesian, and CVT generator point distributions to projectile impacts at increasing speed.

Table 6 depicts the diverse family of damage patterns that result from controlling the impact speed and the computational

mesh. At the largest (200 m/s) and smallest (50 m/s) impact speeds, these simulations qualitatively show some agreement on the overall amount of damage incurred by the target and the size of fragments in the debris field. At the intermediate speed (100 m/s), the fracture patterns that are obtained differ substantially, with the simulations using Cartesian grids showing a significantly lower level of overall damage and larger fragment sizes than the simulations based on the CVT generator mesh. However, it is the CVT mesh that appears to most resemble to the high resolution ($m = 4$) models in the mesh refinement study.

3.4.3. Variety in irregular grids

To demonstrate that the irregular grid results in the previous section are typical, we repeat the simulations using several mesh instances in Table 7. These runs have an impact speed of 100 m/s, time step 10^{-8} s, and the same number of grid points (corresponding to the cubic Cartesian grid with $m = 3$). While there is variation in the fracture patterns, the fragment size distribution and the average damage are relatively consistent across runs.

4. Summary and conclusion

This work identified several meshing issues that arise in simulating peridynamic models. We began with a nonlocal elliptic boundary value problem, and manufactured a solution to facilitate analysis of a numerical scheme. Using a one-dimensional example, we illustrated the role of the model parameters, and linked periodic trends in the solution quality indicators to the interaction processing procedure. The two-dimensional example presented an opportunity to investigate multiple "uniform" quadrature point placement strategies. In this case, we found that a square Cartesian grid and a CVT generators support approximate solutions with

Table 7

Multiple realizations of the irregular grid types demonstrate the variety of fracture patterns that each supports. All simulations contain the same number of grid points (corresponding to a simple cubic grid with $m = 3$), use an impact velocity of 100 m/s, and time step $\Delta t = 10^{-8}$ s.

	Perturbed simple cubic	Centroidal Voronoi generators
Trial 1	Avg. Damage 0.2032	Avg. Damage 0.3624
Trial 2	Avg. Damage 0.2008	Avg. Damage 0.3968
Trial 3	Avg. Damage 0.2012	Avg. Damage 0.3562
Trial 4	Avg. Damage 0.2063	Avg. Damage 0.3938
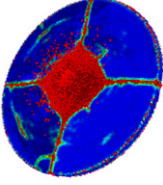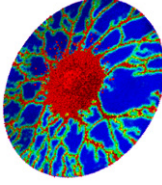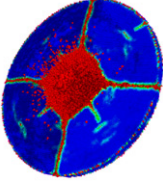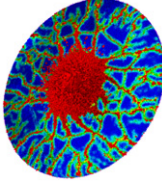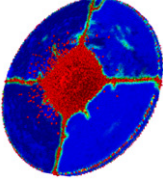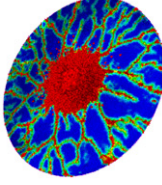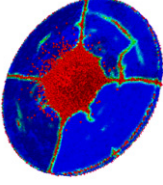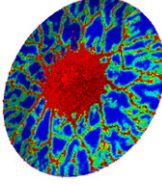
similar accuracy. However, small perturbations in the quadrature point positions have little effect on the accuracy of CVT mesh solutions, but result in an immediate loss of quality for solutions on square grids.

We then exercised the full bond-based peridynamic theory of mechanics in a impact simulation with brittle fracture. We provided evidence that the time and space domains contained sufficient detail, then demonstrated how the computational mesh exerts influence on the outcome of the simulations at intermediate resolutions. The regularity of the cubic meshes was problematic, resulting in cracks that propagate along lines of symmetry in the mesh, while fracture patterns on the CVT generators contained complex branching patterns that compared favorably to the results obtained at higher resolutions. Repeated simulations of the irregular grids displayed noticeably different crack paths, but represent qualitatively similar behaviors.

The core of any peridynamic solution scheme is a quadrature method that integrates nonlocal interactions within the peridynamic horizon. Improvements to the accuracy of a quadrature scheme may be obtained through modifying the number, weighting, or position of sample points. This work shows that careful placement of grid points seems to eliminate any obvious signs of mesh sensitivity without incurring additional computational costs within the simulation. This is an important result because, in many cases, the added cost of generating point distributions (which was several hours for the grids used in Section 3) is amortized over several simulation runs that share the same geometry. Because we have attempted to limit the scope of this work to investigating quadrature point placement, we have neglected the potential gains in accuracy that are possible using a so-called "partial volume method" (e.g. [9,13]). A partial volume method can improve integration accuracy by including assumptions about the geometric arrangement of sample points within the solution scheme, but care must be taken so the new method does not introduce additional bias or errors into the simulation. Combined, it is hoped that changing the position and weights of quadrature points will lead to improved quadrature schemes without resorting to increasing the number of quadrature points.

Peridynamic theory shows great promise in describing materials phenomena that include evolving discontinuities. To fully realize this promise it will be important to develop strategies that ensure the computational mesh exerts minimal interference on the outcome of a simulation. It is hoped that this work is progress towards that goal, and helps others in developing successful models that accurately mimic the behavior of true mechanical systems.

Acknowledgments

Appendix A. Integration error

The integration error expression (19) is obtained by combining Eqs. (10) and (17),

$$b(x_i) = \sum_{j=i+1}^{i+\lfloor m \rfloor} (x_j + x_i) \left| x_j - x_i \right|^{1-P} \Delta x$$
$$- \sum_{j=i-\lfloor m \rfloor}^{i-1} (x_j + x_i) \left| x_j - x_i \right|^{1-P} \Delta x \tag{A.1}$$

where a uniform discretization has been introduced to divide the one-dimensional domain into $m = \delta/\Delta x$ sub-intervals of width Δx. We select an origin so that $x_i = i\Delta x$,

$$b(x_i) = (\Delta x)^{3-P} \left[\sum_{j=i+1}^{i+\lfloor m \rfloor} (j+i) \left| j - i \right|^{1-P} \right.$$
$$\left. - \sum_{j=i-\lfloor m \rfloor}^{i-1} (j+i) \left| j - i \right|^{1-P} \right], \tag{A.2}$$

then merge the two summations by shifting their limits,

$$b(x_i) = (\Delta x)^{3-P} \sum_{j=i+1}^{i+\lfloor m \rfloor} \left[(j+i) \left| j - i \right|^{1-P} \right.$$
$$\left. - (j+i-\lfloor m \rfloor - 1) \left| j - i - \lfloor m \rfloor - 1 \right|^{1-P} \right]. \tag{A.3}$$

Table B.8

Total serialized runtimes for the impact simulations in Section 3. The actual simulations are run in parallel using OpenMP, so these timings include a small overhead cost that would not be present in a single processor run. The represented grid types are simple cubic (SC), simple cubic with random perturbation (RND), and centroidal Voronoi generators (CVT).

Impact velocity (m/s)	Time step (s)	Grid type	Resolution (m-value)	Run time
100	0.5×10^{-8}	SC	2	217 min 18.922 s
100	1.0×10^{-8}	SC	2	107 min 12.683 s
100	2.0×10^{-8}	SC	2	49 min 52.611 s
100	0.5×10^{-8}	SC	3	1864 min 10.379 s
50	1.0×10^{-8}	SC	3	1921 min 05.558 s
100	1.0×10^{-8}	SC	3	932 min 46.746 s
100	2.0×10^{-8}	SC	3	462 min 53.558 s
200	1.0×10^{-8}	SC	3	384 min 45.274 s
100	1.0×10^{-8}	CVT	3	939 min 13.863 s
100	1.0×10^{-8}	CVT	3	919 min 52.121 s
100	1.0×10^{-8}	CVT	3	938 min 00.665 s
100	1.0×10^{-8}	CVT	3	917 min 13.780 s
100	1.0×10^{-8}	RND	3	935 min 56.995 s
100	1.0×10^{-8}	RND	3	937 min 02.418 s
100	1.0×10^{-8}	RND	3	936 min 20.317 s
100	1.0×10^{-8}	RND	3	933 min 43.913 s
100	0.5×10^{-8}	SC	4	6491 min 27.189 s
100	1.0×10^{-8}	SC	4	3253 min 52.351 s
100	2.0×10^{-8}	SC	4	1629 min 47.724 s

Finally, we define $k = j - i$ and replace Δx using its definition,

$$b(x_i) = \left(\frac{\delta}{m}\right)^{3-P} \sum_{k=1}^{\lfloor m \rfloor} \left[(2i+k) \, |k|^{1-P} \right.$$
$$\left. - (2i + k - \lfloor m \rfloor - 1) \, |k - \lfloor m \rfloor - 1|^{1-P} \right], \qquad (A.4)$$

which achieves the result.

Appendix B. Simulation runtimes

See Table B.8.

References

[1] S.A. Silling, Journal of the Mechanics and Physics of Solids 48 (2000) 175.
[2] S. Silling, M. Epton, O. Weckner, J. Xu, E. Askari, Journal of Elasticity 88 (2007) 151.
[3] S. Silling, R. Lehoucq, Peridynamic Theory of Solid Mechanics, in: Advances in Applied Mechanics, vol. 4, Elsevier, 2010, p. 73.
[4] M. Gunzburger, R.B. Lehoucq, Multiscale Modeling and Simulation 8 (2010) 1581.
[5] Q. Du, M. Gunzburger, R.B. Lehoucq, K. Zhou, Mathematical Models and Methods in Applied Sciences 23 (2013) 493.
[6] S. Silling, E. Askari, Computers and Structures 83 (2005) 1526.
[7] E. Emmrich, O. Weckner, Mathematical Modelling and Analysis 12 (2007) 17.
[8] E. Emmrich, O. Weckner, Mathematics and Mechanics of Solids 12 (2007) 363.
[9] M.L. Parks, R.B. Lehoucq, S.J. Plimpton, S.A. Silling, Computer Physics Communications 179 (2008) 777.
[10] R.W. Macek, S.A. Silling, Finite Elements in Analysis and Design 43 (2007) 1169.
[11] X. Chen, M. Gunzburger, Computer Methods in Applied Mechanics and Engineering 200 (2011) 1237.
[12] F. Bobaru, M. Yang, L.F. Alves, S.A. Silling, E. Askari, J. Xu, International Journal for Numerical Methods in Engineering 77 (2009) 852.
[13] F. Bobaru, Y.D. Ha, International Journal for Multiscale Computational Engineering 9 (2011) 635.
[14] Y. Ha, F. Bobaru, International Journal of Fracture 162 (2010) 229.
[15] Y.D. Ha, F. Bobaru, Engineering Fracture Mechanics 78 (2011) 1156.
[16] Q. Du, M. Gunzburger, R. Lehoucq, K. Zhou, SIAM Review 54 (2012) 667.
[17] F. Bobaru, W. Hu, International Journal of Fracture 176 (2012) 215.
[18] S. Silling, R. Lehoucq, Journal of Elasticity 93 (2008) 13.
[19] B. Aksoylu, M.L. Parks, Applied Mathematics and Computation 217 (2011) 6498.
[20] F. Bobaru, M. Duangpanya, International Journal of Heat and Mass Transfer 53 (2010) 4047.
[21] F. Bobaru, M. Duangpanya, Journal of Computational Physics 231 (2012) 2764.
[22] N. Burch, R. Lehoucq, International Journal for Multiscale Computational Engineering 9 (2011) 661.
[23] P. Seleson, M. Parks, International Journal for Multiscale Computational Engineering 9 (2011) 689.
[24] E. Anderson, Z. Bai, C. Bischof, S. Blackford, J. Demmel, J. Dongarra, J. Du Croz, A. Greenbaum, S. Hammarling, A. McKenney, D. Sorensen, LAPACK Users' Guide, third ed., Society for Industrial and Applied Mathematics, Philadelphia, PA, 1999.
[25] M.L. Parks, P. Seleson, S.J. Plimpton, R.B. Lehoucq, S.A. Silling, Peridynamics with LAMMPS: a user guide v0.2 Beta, Technical Report SAND2010-5549, Sandia National Laboratories, 2010.
[26] W. Hu, Y.D. Ha, F. Bobaru, International Journal for Multiscale Computational Engineering 9 (2011) 707.
[27] W. Hu, Y.D. Ha, F. Bobaru, Computer Methods in Applied Mechanics and Engineering 217–220 (2012) 247.
[28] P. Seleson, S. Beneddine, S. Prudhomme, Computational Materials Science 66 (2013) 34.
[29] Q. Du, V. Faber, M. Gunzburger, SIAM Review 41 (1999) 637.
[30] Q. Du, M. Gunzburger, L. Ju, Numerical Mathematics: Theory, Methods and Applications 3 (2010) 119.
[31] Q. Du, M. Gunzburger, L. Ju, Computer Methods in Applied Mechanics and Engineering 191 (2002) 1349.
[32] S. Lloyd, IEEE Transactions on Information Theory 28 (1982) 129.